P. Lunghi, M. Lavagna, R. Armellin
A Semi-Analytical Guidance Algorithm for Autonomous Landing
Advances in Space Research, Vol. 55, N. 11, 2015, p. 2719-2738
doi:10.1016/j.asr.2015.02.022

A Semi-Analytical Guidance Algorithm for Autonomous Landing

Paolo Lunghi[1,*], Michèle Lavagna[2]

Aerospace Science and Technology Department, Politecnico di Milano, Via La Masa 34, 20156 Milano, Italy

Roberto Armellin[3]

Aeronautics, Astronautics and Computational Engineering Academic Unit, University of Southampton, Highfield Campus, Southampton SO17 1BJ - UK

Abstract

One of the main challenges posed by the next space systems generation is the high level of autonomy they will require. Hazard Detection and Avoidance is a key technology in this context. An adaptive guidance algorithm for landing that updates the trajectory to the surface by means of an optimal control problem solving is here presented. A semi-analytical approach is proposed. The trajectory is expressed in a polynomial form of minimum order to satisfy a set of boundary constraints derived from initial and final states and attitude requirements. By imposing boundary conditions, a fully determined guidance profile is obtained, function of a restricted set of parameters. The guidance computation is reduced to the determination of these parameters in order to satisfy path constraints and other additional constraints not implicitly satisfied by the polynomial formulation. The algorithm is applied to two different scenarios, a lunar landing and an asteroidal landing, to highlight its general validity. An extensive Monte Carlo test campaign is conducted to

*Corresponding author

Email addresses: paolo.lunghi@polimi.it (Paolo Lunghi), michelle.lavagna@polimi.it (Michèle Lavagna), roberto.armellin@soton.ac.uk (Roberto Armellin)

[1]PhD Candidate

[2]Associate Professor

[3]Lecturer

verify the versatility of the algorithm in realistic cases, by the introduction of attitude control systems, thrust modulation, and navigation errors. The proposed approach proved to be flexible and accurate, granting a precision of a few meters at touchdown.

Keywords: autonomous landing, optimal guidance, powered descent, trajectory optimization

1. Introduction

In last years, a renewed interest in planetary exploration has brought to the realization of several missions, especially towards Mars, culminated with the landing of the rover Curiosity in August 2012. Together with Mars, the Moon is a main destination for exploration. The European Space Agency has conducted several studies concerning a possible unmanned lunar lander (Carpenter et al., 2012), while NASA is planning to send humans back to space. ESA will supply the Orion/MPCV European Service Module (ESM) for the 2018 unmanned Exploration-1 Mission, including ground and flight operation support (Marshall and Norris, 2013). Targets for the subsequent manned Exploration-2 and 3 missions are under study, including Near-Earth Asteroids (NEA) and the Moon as possible destinations. Provisions for the construction and delivery of a second ESM have been taken. Recently ESA and the Russian federal space agency, Roscosmos, have signed a formal agreement to work in partnership on the ExoMars programme towards the launch of two missions in 2016 and 2018, with the goal to bring a rover on Mars surface. In addition to mission to planets and their moons there is a strong interest in visiting small bodies as asteroids and comets. A typical high-autonomy scenario is the close approach to a low-gravity object, finalized to either touch and go operations or landing. The ESA Rosetta probe, launched in March 2004, have performed a rendezvous with the comet 67P/Churyumov-Gerasimenko in August 2014. The release of the lander Philae, with the objective to collect and on-board analyze samples of comet's soil, has been successfully performed the next 12th November (Geurts et al., 2014). The OSIRIS-REx spacecraft, planned by NASA for launch in 2016, will travel to the NEA Bennu, study it in detail, and bring back a sample to Earth (Gal-Edd and Cheuvront, 2014). MarcoPolo-R, a project with similar objectives, has been studied by European Space Agency as M-class candidate mission for the launch in 2022 (Michel et al., 2014). Recently, in the FY2014 budget proposal, NASA has

included a plan to robotically capture a small NEA and redirect it safely to a stable orbit in the Earth-moon system where astronauts can visit and explore it (Condon and Williams, 2014). ESA is studying with NASA the AIDA mission including ESA's AIM and NASA's DART spacecraft, to be launched to rendezvous with the Didymos binary asteroid. To be launched in 2020, AIM will rendezvous and release a lander to one of the bodies in 2022 (Cheng, 2013).All the examples mentioned above share the common problem of designing a landing on a celestial body. The landing phase is a critical phase, being usually a single point of failure for the mission success.

During last decades, several improvements in automatic landing precision have been implemented, but the relative uncertainty of the landing dispersion still imposes strict requirements on the landing site selection. On the other hand, scientifically relevant places may be associated with hazardous terrain features or confined in very limited areas; in other cases there is no possibility to completely characterize a predefined landing area with the required accuracy. Moreover, in the case of planetary landing, the short duration of the landing phase, together with telecommunications delays, makes a continuous control from the ground impossible. Even in cases where the long duration of the maneuver allows a certain degree of remote control (such as the case of proximity maneuvers around low gravity bodies) high accuracy is still impossible without an on-board autonomous guidance system (Berry et al., 2013), as well as efficient counteraction to unexpected events or failures, as demonstrated by the uncontrolled bounce of the ESA lander Philae during the recent landing on the comet 67P.

This is why precise and autonomous landing capability is a key feature for the next space systems generation. The system must perform high precision relative navigation, and seek and identify a reachable and safe landing site; then, it needs to recalculate a pinpoint feasible trajectory toward the target. The minimization of the propellant consumption is a goal of every space mission, as it allows a reduction in launch mass or an increase in payload, and thus in the scientific return of the mission. Also, a fuel optimal approach in hazard avoidance computation contributes to maximize the attainable landing area, consequently increasing the chances to find a safe landing site. That is why propellant minimization can be considered as an ideal criterion in divert trajectory design. On the other hand, numerical optimization implies usually heavy computation with no guarantee of convergence.

Different approaches at the problem have been adopted during the years. A trajectory based on a quartic polynomial in time, with no optimization

involved, was used during the Apollo missions (Klumpp, 1974). A derivative of the Apollo lunar descent guidance has been still considered in recent years for the Mars Science Laboratory (MSL) (Wong et al., 2002). Various other approaches to obtain both numerical and approximate solutions of the pinpoint landing terminal guidance problem have been proposed over the last few years. In Topcu et al. (2005) the first-order necessary conditions for the problem are developed, and it is shown that the optimal thrust profile has a maximum-minimum-maximum structure. Direct numerical methods for trajectory optimization have been widely investigated, not requiring the explicit consideration of the necessary conditions and with better convergence properties (Betts, 1998). These methods have been used together with Chebyshev pseudospectral techniques, to allow the reduction of the number of the optimization variables (Fahroo and Ross, 2002). Also convex programming has been proposed to guarantee the convergence of the optimization; this approach, coupled with direct collocation methods, has proved that the size of the region of feasible initial states, for which there exist feasible trajectories, can be increased drastically (more than twice) compared to the traditional polynomial-based guidance approaches, but at the price of a higher computational cost (Açikmeşe and Ploen, 2007). This method has been coupled with a minimum-landing-error approach, in order to compute a landing trajectory even in case a feasible solution for the selected landing site is not found (Blackmore et al., 2010).

In the case of asteroids and comets, landing and close proximity operations present some peculiarities, due to their small size and irregular shape. In particular, the gravitational acceleration is very weak and variable in function of the relative position of the spacecraft respect to the target. Due to that, orbits are generally complex and non periodic, and stable only in certain regions (Lara and Scheeres, 2002). Zero Emission Effort/Zero Emission Velocity guidance had been proved to produce a good approximation of the fuel-optimal trajectory in close proximity maneuvers around asteroids (Hawkins et al., 2012), and it has been applied together with high-order sliding mode control to increase robustness to disturbances and unmodeled dynamics (Furfaro et al., 2013a,b).

In this work a guidance algorithm capable to dynamically recompute and correct the landing trajectory during the descent is developed, allowing the on-board choice of the landing site, as required by systems that have to operate in full autonomy. An innovative semi-analytical approach is proposed: the trajectory is parameterized in a polynomial form, depending

only on a few parameters that can be efficiently optimized by a simple derivative-free optimization algorithm. Traditional closed-form guidance schemes (such as Apollo guidance, E-guidance) are sub-optimal and do not include explicitly path constraints, potentially leading to infeasible trajectories. On the other hand, fully numerical methods, although extremely flexible in terms of optimality and constraints evaluation, require the handling of tens of optimization variables or complex gradient based optimization techniques, and thus they are computationally intensive (Gerth and Mooij, 2014). With the proposed approach, the feasibility region is increased with respect to traditional polynomial algorithms, avoiding at the same time the higher computational cost of complex optimization methods, being the number of variables to be optimized very low. Furthermore, additional parameters allow us to include path constraints usually not taken into account by traditional guidance algorithms. As a result a simple, efficient, and nearly-optimal guidance law is obtained.

This paper is organized as follows: in Sec. 2 the general logic of the proposed algorithm is presented. Then, it is formalized in Sec. 3 for the planetary landing case, and in Sec. 4 for a NEA close approach. Sec. 5 presents some result obtained in simulations of a lunar and an asteroidal landing. Monte Carlo simulations are presented to assess the effectiveness of the proposed method. Conclusions and implications of the obtained results are discussed in Sec. 6.

2. Semi-analytical Polynomial Guidance Approach

The retargeting problem, as part of a Hazard Detection and Avoidance (HDA) system, involves the last part of the landing phase only. In order to handle a wide range of cases, the proposed algorithm presents a general approach, from slow (low-gravity objects) to fast (planetary landing) dynamics. The implemented guidance is based on the following scheme:

1. The system translational dynamics are identified and expressed in the general form:

$$\begin{cases} \dot{\mathbf{r}} = \mathbf{v} \\ \dot{\mathbf{v}} = \mathbf{f}(\mathbf{r}, \mathbf{v}, m, \mathbf{T}) \\ \dot{m} = g(\mathbf{T}) \end{cases} \tag{1}$$

where $\mathbf{r}$ is the position vector, $\mathbf{v}$ is the velocity vector, m is the mass of the spacecraft, and $\mathbf{T}$ is the thrust vector. $\mathbf{f}(\mathbf{r}, \mathbf{v}, m, \mathbf{T})$ and $g(\mathbf{T})$ are

generic functions of states and thrust.

2. The boundary constraints are defined. The retargeting starts at the time t_0 when the full spacecraft state $\mathbf{r}_0$, $\mathbf{v}_0$, and m_0 is supposed to be known. At final time t_f constraints on both position $\mathbf{r}_\mathrm{f}$ and velocity $\mathbf{v}_\mathrm{f}$ are considered. Additional boundary constraints on initial and final acceleration can arise from the actual system architecture, depending on propulsion and attitude control systems requirements. Initial acceleration is expressed as function of initial thrust magnitude and, when needed, initial spacecraft attitude.
3. The acceleration profile is expressed in a polynomial form in time, of minimum order to satisfy the boundary constraints. By inverse dynamics, a complete control profile is obtained, function of time-of-flight and additional parameters which are problem dependent.
4. The problem is reduced to find the values of these parameters, according to any additional constraint not implicitly satisfied by the polynomial formulation, minimizing the fuel consumption. Representing as $\mathbf{x}$ the vector of optimization parameters, the cost function is $f(\mathbf{x}) = m(t_0) - m(t_\mathrm{f})$, and the problem can be expressed in the form:

$$\min_{\mathbf{x}} f(\mathbf{x}) \text{ such that } \begin{cases} \mathbf{x}_L \leq \mathbf{x} \leq \mathbf{x}_U \\ \mathbf{c}_L \leq \mathbf{c}(\mathbf{x}) \leq \mathbf{c}_U \end{cases} \tag{2}$$

The search space for the optimization variables is defined by upper and lower bounds, $\mathbf{x}_U$ and $\mathbf{x}_L$ respectively. These are called *Box Constraints*. The elements of $\mathbf{c}(\mathbf{x})$ in Eq. (2) are generally nonlinear functions of the optimization variables, also bounded between lower and upper limits $\mathbf{c}_L$ and $\mathbf{c}_U$. These constraints need to be satisfied during all the landing maneuver, and they are called *Path Constraints*.

3. Lunar Landing: Problem Formulation

A planetary landing is characterized by fast dynamics. The expected time of flight is in the order of magnitude of 1 min, and the mass is supposed to significantly change during the maneuver.

3.1. Problem Statement

In the case of a planetary landing, distances, for both downrange and altitude, are small compared to the planet's radius; thus, the assumption

of a constant gravity field with flat ground is appropriate. Furthermore, aerodynamic forces are neglected. In fact the eventual presence of atmosphere (especially with low density, as in the case of Mars) could be negligible due to the relative low velocity (on the order of $100\,\mathrm{m\,s^{-1}}$), and the associated forces can be treated as disturbances (Açikmeşe and Ploen, 2007).

The translational dynamics of the spacecraft are expressed in a *Ground Reference System* (GRS, see Fig. 1), where x is the altitude, y is called the *Downrange* direction and z is the *Crossrange* direction. Dynamics are described by the equations

$$\begin{cases} \dot{\mathbf{r}} = \mathbf{v} \\ \dot{\mathbf{v}} = \dfrac{\mathbf{T}}{m} + \mathbf{g} \\ \dot{m} = -\dfrac{T}{I_{\mathrm{sp}} g_0} \end{cases} \tag{3}$$

where $\mathbf{g}$ is the constant acceleration of gravity vector of the planet, I_{sp} the specific impulse of the main engine, and g_0 the standard gravity acceleration on Earth. The thrust net magnitude is indicated with $T = \|\mathbf{T}\|$.

In this system, the thrust vector acts as control variable. The mass equation is linked to the control acceleration by the thrust-to-mass ratio $\mathbf{P}$:

$$\mathbf{P} = \mathbf{T}/m = \dot{\mathbf{v}} - \mathbf{g} \tag{4}$$

Then, the mass equation in system (3) can be rewritten as

$$\dot{m} = -\frac{P}{I_{\mathrm{sp}} g_0} m \tag{5}$$

which is a first order linear ordinary differential equation whose solution is

$$m(t) = m_0 \exp\left(- \int_{t_0}^{t} \frac{P(\tau)}{I_{\mathrm{sp}} g_0} d\tau \right) \tag{6}$$

At the time t_0 the initial states $\mathbf{r}_0$, $\mathbf{v}_0$ and m_0 are supposed to be known. At the end of the maneuver, at time t_{f}, final states $\mathbf{r}_{\mathrm{f}}$ and $\mathbf{v}_{\mathrm{f}}$ are required. Then, the optimal guidance problem is to find a control profile $\mathbf{T}(t)$, to bring the system from the initial to the target final states, compatibly with all the

constraints imposed by the actual system architecture.

3.2. Parametric Trajectory Formulation

The main thruster is assumed to be tightly connected to the spacecraft body. Thus, the direction of the thrust vector is determined directly by the spacecraft attitude. The spacecraft attitude is expressed relatively to an auxiliary reference system, called *Flight Reference System* (FRS), defined by the unit vectors $[\mathbf{x}_\mathrm{f}\ \mathbf{y}_\mathrm{f}\ \mathbf{z}_\mathrm{f}]^T$ (see Fig. 2), centered in the center of mass of the spacecraft, the $\mathbf{x}_\mathrm{f}$ axis pointing toward the downrange direction (y in GRS), the $\mathbf{z}_\mathrm{f}$ axis pointing downwards, an the $\mathbf{y}_\mathrm{f}$ axis forming a right-handed triad.

Attitude is defined as the rotation from FRS to the *Body-Fixed Reference Frame* (BRF). The body axes $[\mathbf{x}_b\ \mathbf{y}_b\ \mathbf{z}_b]^T$ are assumed to be defined as in Fig. 3, where the $\mathbf{x}_\mathrm{b}$ direction is called *Roll* axis, $\mathbf{y}_\mathrm{b}$ is the *Pitch* axis and $\mathbf{z}_\mathrm{b}$ is the *Yaw* axis. The rotation is expressed in Euler angles, in the 231 form, where θ (pitch angle) is the first rotation around $\mathbf{y}_\mathrm{b}$, ψ (yaw angle) is the second rotation about $\mathbf{z}_\mathrm{b}$, and ϕ (roll angle) is the third rotation around $\mathbf{x}_\mathrm{b}$. The 231 form is preferred to the more traditional 321, because it avoids the presence of singularities in the angles determination, in the field of application of the landing phase. The attitude with respect the flight reference frame is expressed by the cosine director matrix

$$\mathrm{A_b} = \begin{bmatrix} c\psi c\theta & s\psi & -c\psi s\theta \\ -c\phi s\psi c\theta + s\phi s\theta & c\phi c\psi & c\phi s\psi s\theta + s\phi c\theta \\ s\phi s\psi c\theta + c\phi s\theta & -s\phi c\psi & -s\phi s\psi s\theta + c\phi c\theta \end{bmatrix} \tag{7}$$

where c and s are the abbreviated forms for cos and sin.

The rotation of the flight reference frame with respect to the ground is constant and expressed by the matrix

$$\mathrm{A_f} = \begin{bmatrix} 0 & 0 & -1 \\ 1 & 0 & 0 \\ 0 & -1 & 0 \end{bmatrix} \tag{8}$$

Following these assumptions, the thrust vector can be represented as:

$$\mathbf{T}(t) = \mathrm{A_f^T A_b^T} \begin{bmatrix} -T(t) \\ 0 \\ 0 \end{bmatrix} = -T(t) \begin{bmatrix} \cos\psi(t)\sin\theta(t) \\ \cos\psi(t)\cos\theta(t) \\ -\sin\psi(t) \end{bmatrix} \tag{9}$$

By substituting Eq. (9) in Eqs. (3) the system can be written in its scalar form as:

$$\begin{cases} \dot{x} = v_{\mathrm{x}} \\ \dot{y} = v_{\mathrm{y}} \\ \dot{z} = v_{\mathrm{z}} \\ \dot{v}_{\mathrm{x}} = -T\dfrac{\cos\psi\sin\theta}{m} + g_{\mathrm{x}} \\ \dot{v}_{\mathrm{y}} = -T\dfrac{\cos\psi\cos\theta}{m} \\ \dot{v}_{\mathrm{z}} = T\dfrac{\sin\psi}{m} \\ \dot{m} = -\dfrac{T}{I_{\mathrm{sp}}g_0} \end{cases} \tag{10}$$

Eqs. (10) show that the system is not affected by the roll angle ϕ. Since that, ϕ is always considered as null. In this form, the control variables consist of the thrust magnitude T, the pitch angle θ and the yaw angle ψ; anyway, the attitude profile is not a completely free parameter: pitch and yaw angles at time t_0 are known and fixed. This imposes an additional boundary constraint on the initial acceleration, which now depends only on the initial thrust magnitude:

$$\dot{\mathbf{v}}_0 = -\frac{T(t_0)}{m_0}\begin{bmatrix}\cos\psi_0\sin\theta_0 \\ \cos\psi_0\cos\theta_0 \\ -\sin\psi_0\end{bmatrix} + \begin{bmatrix} g_{\mathrm{x}} \\ 0 \\ 0 \end{bmatrix} \tag{11}$$

Moreover, at the end of the maneuver, the lander's attitude is required to be aligned with the local vertical on the Target Landing Site (TLS). This boundary constraint is expressed through the equation

$$\dot{\mathbf{v}}(t_{\mathrm{f}}) \times \hat{\mathbf{n}}_{\mathrm{LS}} = \mathbf{0} \tag{12}$$

where $\hat{\mathbf{n}}_{\mathrm{LS}}$ is the unit vector normal to the planetary surface at the TLS. In case of flat surface, $\hat{\mathbf{n}}_{\mathrm{LS}}$ is aligned with the x axis of the ground reference frame (see Fig. 1), and Eq. (12) reduces to

$$\dot{v}_{\mathrm{y}}(t_{\mathrm{f}}) = \dot{v}_{\mathrm{z}}(t_{\mathrm{f}}) = 0 \tag{13}$$

A total of 17 boundary constraints are available for position, velocity and acceleration components: 6 on initial states, 3 on initial acceleration (function

of initial thrust magnitude), 6 on target final states and 2 on final acceleration due to final attitude requirements

$$\begin{cases} \mathbf{r}(t_0) = \mathbf{r}_0 \\ \mathbf{v}(t_0) = \mathbf{v}_0 \\ \dot{\mathbf{v}}(t_0) = \mathbf{f}(T_0, \theta_0, \psi_0) \\ \mathbf{r}(t_\mathrm{f}) = \mathbf{r}_\mathrm{f} \\ \mathbf{v}(t_\mathrm{f}) = \mathbf{v}_\mathrm{f} \\ \dot{\mathbf{v}}(t_\mathrm{f}) = [free, 0, 0]^T \end{cases} \tag{14}$$

The 3 components of the acceleration can be expressed in a polynomial form. The minimum order needed to satisfy boundary constraints is 2 for the vertical axis, 3 for the horizontal components:

$$\dot{\mathbf{v}}(t) = \begin{bmatrix} \dot{v}_\mathrm{x} \\ \dot{v}_\mathrm{y} \\ \dot{v}_\mathrm{z} \end{bmatrix} = \begin{bmatrix} \dot{v}_{0\mathrm{x}} + c_{1\mathrm{x}} t + c_{2\mathrm{x}} t^2 \\ \dot{v}_{0\mathrm{y}} + c_{1\mathrm{y}} t + c_{2\mathrm{y}} t^2 + c_{3\mathrm{y}} t^3 \\ \dot{v}_{0\mathrm{z}} + c_{1\mathrm{z}} t + c_{2\mathrm{z}} t^2 + c_{3\mathrm{z}} t^3 \end{bmatrix} \tag{15}$$

Integrating the acceleration two times, and applying boundary constraints, the trajectory becomes function of t_f and T_0. Once the acceleration profile is defined, the thrust-to-mass ratio can be obtained from Eq. (4) and the thrust profile is:

$$\mathbf{T} = m\mathbf{P} \tag{16}$$

The mass profile is obtained by solving Eq. (6). The analytical calculation of the integral exponent is complex, but can be easily attainable through numerical integration. From the thrust unit vector $\hat{\mathbf{n}}_\mathrm{T} = \mathbf{T}/\|\mathbf{T}\|$ a complete guidance profile, in terms of Euler angles and thrust magnitude, is obtained, function of initial thrust magnitude T_0 and final time t_f:

$$\begin{cases} \theta = \tan^{-1}\left(\hat{n}_{\mathrm{Tx}}/\hat{n}_{\mathrm{Ty}}\right) & -\pi \leq \theta \leq 0 \\ \psi = \tan^{-1}\left(\hat{n}_{\mathrm{Tz}}\left(\hat{n}_{\mathrm{Tx}}^2 + \hat{n}_{\mathrm{Ty}}^2\right)^{-0.5}\right) & -\dfrac{\pi}{2} \leq \psi \leq \dfrac{\pi}{2} \\ \phi = 0 \end{cases} \tag{17}$$

The free parameter t_f can be replaced by the time-of-flight $t_\mathrm{tof} = t_\mathrm{f} - t_0$.

3.3. Trajectory Constraints

Box constraints, path constraints and any other additional constraint not implicitly satisfied by the polynomial formulation are written in the form of Eq. (2). For this case, $\mathbf{x} = [t_{\text{tof}}, T_0]^T$.

The time-of-flight must be greater than zero, whereas its theoretical upper limit is determined by the maximum amount of fuel on board m_{fuel}:

$$0 \leq t_{\text{tof}} \leq t_{\max} = m_{\text{fuel}} \frac{I_{\text{sp}} g_0}{T_{\min}} \tag{18}$$

The thrust magnitude is bounded to the thrust actually available on-board:

$$0 < T_{\min} \leq T_0 \leq T_{\max} \tag{19}$$

Boundaries on thrust are applied also as path constraint:

$$T_{\min} \leq T(t) \leq T_{\max} \tag{20}$$

Euler angles rate of change is subject to the actual control torques M_{Cmax} available by the Attitude Control System (ACS). The extrapolation of the exact torques from angles is not immediate, due to coupled terms in the attitude dynamics. The objective is to characterize such a rotational rate constraint without coupling the problem to the rotational dynamics, to save computation time. Torques are approximated by the decoupled term due to the angular acceleration. This is accurate in case of small angles and low angular speed. This approximation can be exploited to estimate the bounds we need:

$$-\frac{\rho M_{\text{Cmax}}}{I_{\max}} \leq \ddot{\theta}(t) \leq \frac{\rho M_{\text{Cmax}}}{I_{\max}} \tag{21}$$

$$-\frac{\rho M_{\text{Cmax}}}{I_{\max}} \leq \ddot{\psi}(t) \leq \frac{\rho M_{\text{Cmax}}}{I_{\max}} \tag{22}$$

in which $I_{\max}$ is the maximum moment of inertia at initial time t_0. In this way, the on-board calculation of inertia properties can be avoided, and a margin of safety in the torques calculation is introduced. An additional safety margin $0 < \rho < 1$ can be applied.

In a feasible landing path, altitude is always greater than zero. This constraint can be improved considering a *Glide-Slope Constraint*. In this case the lander is required to remain in a cone defined by the maximum

slope angle $\delta_{\max}$, as showed in Fig. 4. This constraint has a dual purpose: it assures that the the lander does not penetrate the ground, even in presence of bulky terrain features near the landing site; at the same time it limits the angle of view on the target. In fact, the performances of vision-based navigation systems depend on inclination between the trajectory and the ground (Flandin et al., 2010; Riedel et al., 2010). Following Açikmeşe and Ploen (2007), the constraint takes the form

$$-\infty \leq \|\mathrm{S_g}\mathbf{r}(t)\| + \mathbf{c}_\mathrm{g}^T\mathbf{r}(t) \leq 0 \tag{23}$$

where

$$\mathrm{S_g} = \begin{bmatrix} 0 & 1 & 0 \\ 0 & 0 & 1 \end{bmatrix} \tag{24}$$

$$\mathbf{c}_\mathrm{g}^T = \begin{bmatrix} -\tan\delta_{\max} & 0 & 0 \end{bmatrix} \tag{25}$$

Path constraints need to be satisfied at every time instant during the landing. Pseudospectral techniques allow us to evaluate them discretely. Derivative terms are obtained by the use of the Chebyshev differentiation matrix (Canuto et al., 1988).

Finally, the polynomial formulation does not explicitly consider boundary constraint on mass. This implies the additional constraint

$$m_{\mathrm{dry}} \leq m(t_{\mathrm{tof}}) \leq m_0 \tag{26}$$

3.4. Optimization Problem

The generic optimization problem (2) for planetary landing takes the form:

Find T_0 and t_{tof}, in the domain defined by the inequalities (18) *and* (19)*, that minimize fuel consumption computed by the Eq.* (6)*, subject to constraints* (20)*,* (21)*,* (22)*,* (23) *and* (26)*.*

The optimization can be solved with any nonlinear programming (NLP) solver. The choice of this solver has a huge impact over the final convergence properties and computational time. In order to emphasize the robustness and the simplicity of the semi-analytical polynomial guidance, a very simple method is exploited in all the simulations here presented.

A modified version of the *Compass Search*, enhanced to handle also nonlinear constraints, is adopted. For a detailed description of the classical compass

search method, and its application to nonlinear programming problems, see Kolda et al. (2003).

4. Asteroid/Small Body Landing: Problem Formulation

Relatively low thrust and slow dynamics are typical of maneuvers in low-gravity environment. The maneuver here presented is suitable for both landing and close approach to low-gravity objects such as NEA. The expected time is in the order of magnitude of several thousands of seconds, but with a very limited change in mass.

4.1. Problem Statement

The motion of the spacecraft is modeled in an asteroid-fixed Cartesian frame, centered in the center of mass of the asteroid. Assuming the asteroid rotational rate as constant, the dynamics are described (using the same notation of the planetary landing case) by the well known equations of motion for uniform rotating frames

$$\begin{cases} \dot{\mathbf{r}} = \mathbf{v} \\ \mathbf{a} = \dot{\mathbf{v}} + 2\boldsymbol{\omega} \times \mathbf{v} + \boldsymbol{\omega} \times \boldsymbol{\omega} \times \mathbf{r} \\ \dot{m} = -\dfrac{T}{I_{\mathrm{sp}} g_0} \end{cases} \tag{27}$$

where $\mathbf{a}$ is the acceleration vector and $\boldsymbol{\omega}$ is the asteroid rotational rate vector. A restricted two-body model is considered: the spacecraft mass is assumed to be negligible compared to the asteroid. The adopted reference frame is represented in Fig. 5.

The acceleration vector acting on the spacecraft consists of different contributions

$$\mathbf{a} = \mathbf{g}(\mathbf{r}) + \mathbf{a}_{\mathrm{c}} + \mathbf{d} \tag{28}$$

in which $\mathbf{g}(\mathbf{r})$ is the gravitational acceleration, function of the position in the asteroid reference frame, $\mathbf{a}_{\mathrm{c}}$ is the control acceleration and $\mathbf{d}$ is a term that includes disturbances (such as solar pressure or additional gravity terms due to non uniform density or irregular shape).

The asteroid is modeled as a tri-axial ellipsoid with uniform density ρ. This allows us to analytically evaluate the gravitational component of the

acceleration as the gradient of its potential field $V_g(\mathbf{r})$ (Scheeres, 1994):

$$\mathbf{g}(\mathbf{r}) = -\nabla\big(V_g(\mathbf{r})\big) \tag{29}$$

Other gravity models, such as a polyhedron shape model (Werner and Scheeres, 1996), could be considered without impacting on the proposed guidance algorithm. Assuming the asteroid's rotational rate vector aligned with the z axis, results $\boldsymbol{\omega} = [0, 0, \omega]^T$. Then, the dynamical system can be written in scalar form as

$$\begin{cases} \dot{x} = v_x \\ \dot{y} = v_y \\ \dot{z} = v_z \\ \dot{v}_x = 2\omega v_y + \omega^2 x - \dfrac{\partial V_g}{\partial x} + a_{\mathrm{cx}} + d_x \\ \dot{v}_y = -2\omega v_x + \omega^2 y - \dfrac{\partial V_g}{\partial y} + a_{\mathrm{cy}} + d_y \\ \dot{v}_z = -\dfrac{\partial V_g}{\partial z} + a_{\mathrm{cz}} + d_z \end{cases} \tag{30}$$

As the planetary landing case, the mass equation is linked to the control acceleration that corresponds to the thrust-to-mass ratio:

$$\mathbf{a}_{\mathrm{c}} = \mathbf{T}/m = \mathbf{P} \tag{31}$$

The mass versus time trend is then evaluated with the same solution of Eq. (6).

4.2. Parametric Trajectory Formulation

From Eqs. (30) and (28), the initial derivative of the velocity depends on the initial control acceleration, which is determined by the initial thrust vector $\mathbf{T}_0$ (disturbances are not taken into account in the guidance algorithm). In order to minimize the number of free parameters of the polynomial guidance the initial thrust vector is constrained on the plane defined by $\mathbf{r}_0$ and $\mathbf{r}_f$, as shown in Fig. 6. First a local frame defined by the direction cosines matrix A_0 is defined

$$\mathrm{A}_0 = [\hat{\mathbf{x}}_0 \quad \hat{\mathbf{y}}_0 \quad \hat{\mathbf{z}}_0]^T \tag{32}$$

where

$$\hat{\mathbf{x}}_0 = -\frac{\mathbf{r}_0}{\|\mathbf{r}_0\|} \tag{33}$$

$$\hat{\mathbf{z}}_0 = \frac{\mathbf{r}_\mathrm{f} \times \mathbf{r}_0}{\|\mathbf{r}_\mathrm{f} \times \mathbf{r}_0\|} \tag{34}$$

$$\hat{\mathbf{y}}_0 = \hat{\mathbf{z}}_0 \times \hat{\mathbf{x}}_0 \tag{35}$$

This local frame is aligned with the spacecraft-asteroid direction, and its xy plane contains $\mathbf{r}_0$ and $\mathbf{r}_\mathrm{f}$. By defining a second matrix describing a rotation η_0 around $\hat{\mathbf{z}}_0$

$$\mathrm{A}_{\eta_0} = \begin{bmatrix} \cos\eta_0 & \sin\eta_0 & 0 \\ -\sin\eta_0 & \cos\eta_0 & 0 \\ 0 & 0 & 1 \end{bmatrix} \tag{36}$$

the initial thrust vector $\mathbf{T}_0$ can be expressed as function of initial thrust magnitude T_0 and initial angle of thrust η_0 only

$$\mathbf{T}_0 = \mathrm{A}_0^T \mathrm{A}_{\eta_0}^T \begin{bmatrix} T_0 & 0 & 0 \end{bmatrix}^T \tag{37}$$

The problem is characterized by a set of 15 boundary constraints: 6 on initial states, 3 on initial control acceleration and 6 on the desired final states

$$\begin{cases} \mathbf{r}(t_0) = \mathbf{r}_0 \\ \mathbf{v}(t_0) = \mathbf{v}_0 \\ \dot{\mathbf{v}}(t_0) = \mathbf{f}(T_0, \eta_0) \\ \mathbf{r}(t_\mathrm{f}) = \mathbf{r}_\mathrm{f} \\ \mathbf{v}(t_\mathrm{f}) = \mathbf{v}_\mathrm{f} \end{cases} \tag{38}$$

These constraints are satisfied by expressing the acceleration in a polynomial form. The minimum order needed to satisfy boundary constraints is 3. If $t_0 = 0$:

$$\dot{\mathbf{v}}(t) = \dot{\mathbf{v}}_0 + \mathbf{c}_1 t + \mathbf{c}_2 t^2 + \mathbf{c}_3 t^3 \tag{39}$$

By integrating Eq. (39) as needed, and solving for the boundary constraints, a fully defined trajectory can be determined, depending on 3 parameters: time-of-flight t_tof, initial thrust magnitude T_0, and initial angle of thrust η_0. By solving acceleration equations in the system (30) for $\mathbf{a}_c$ a complete control

acceleration profile is obtained.

4.3. Trajectory Constraints

The search space for the time of flight is defined by

$$0 \leq t_{\text{tof}} \leq \sqrt{\frac{2r_0^2 h_0}{\mu}} \tag{40}$$

in which h_0 is the initial altitude over the asteroid, and μ is its gravitational parameter

$$\mu = G\rho\frac{4\pi}{3}abc \tag{41}$$

with G the universal gravitational constant, and a, b, c semi-axes of the ellipsoid. The adopted upper bound represents the time that the spacecraft would take to cover a distance equal to h_0 in free fall, if subject to a constant acceleration of gravity equal to $\mathbf{g}(\mathbf{r}_0)$. It has no real physical meaning, but it has the proper order of magnitude (2-3 times the optimal t_{tof}) for an efficient optimum search.

The initial thrust magnitude is bounded to the thrust available on-board:

$$-T_{\max} \leq T_0 \leq T_{\max} \tag{42}$$

The initial thrust angle bounds should be large enough to cover every direction in the plane:

$$-\frac{\pi}{2} \leq \eta_0 \leq \frac{\pi}{2} \tag{43}$$

During the landing the required thrust magnitude cannot exceed the limit imposed by the actual engine on board. Since the control action is evaluated in terms of acceleration, the corresponding thrust should depends on the actual spacecraft mass, according to the Newton's second law. Actually, the relatively small fuel consumption in low gravity environments allows us to consider the mass as constant in the constraints evaluation:

$$0 \leq \|\mathbf{a}_{\text{c}}(t)\| \leq \frac{T_{\max}}{m_0} \tag{44}$$

Also in this case, a *Glide-Slope Constraint* is considered. The spacecraft is required to remain in a cone, pointing at the TLS and defined by the maximum slope angle $\delta_{\max}$, as showed in Fig. 7.

Due to the small dimension of the target, it is possible that the maneuver starts from a position that does not satisfy this constraint. In this case is required that the spacecraft remains over a minimum altitude as long as it doesn't enter into the cone. The j-th general constraint on trajectory shape can be represented in the form

$$-\infty \leq \|\mathrm{S}_j \mathbf{r}(t) - \mathbf{b}_j\| + \mathbf{c}_j^T \mathbf{r}(t) + a_j \leq 0 \tag{45}$$

where $\mathrm{S}_j \in \mathbb{R}^{3\times 3}$, $\mathbf{b}_j \in \mathbb{R}^3$, $\mathbf{c}_j \in \mathbb{R}^3$ and $a_j \in \mathbb{R}$. In the case of the glide-slope cone, we have

$$\mathrm{S}_\mathrm{g} = \mathrm{I} - \mathbf{n}\mathbf{n}^T \tag{46}$$

$$\mathbf{b}_\mathrm{g} = \mathrm{S}_\mathrm{g} \mathbf{r}_\mathrm{f} \tag{47}$$

$$\mathbf{c}_\mathrm{g}^T = -\tan(\delta_{\max}) \mathbf{n}^T \tag{48}$$

$$a_\mathrm{g} = -\mathbf{c}_\mathrm{g}^T \mathbf{r}_\mathrm{f}, \tag{49}$$

where $\mathbf{n}$ is the unit vector normal to the ground at the TLS. The constraint on minimum altitude $h_{\min}$ for a tri-axial ellipsoid can be expressed with

$$\mathrm{S}_\mathrm{h} = -\operatorname{diag}\big([\beta\gamma, \alpha\gamma, \alpha\beta]\big) \tag{50}$$

$$\mathbf{b}_\mathrm{h} = 0 \tag{51}$$

$$\mathbf{c}_\mathrm{h}^T = 0 \tag{52}$$

$$a_\mathrm{h} = -\alpha\beta\gamma \tag{53}$$

where $\alpha = a + h_{\min}$, $\beta = b + h_{\min}$ and $\gamma = c + h_{\min}$. Glide-slope cone and minimum altitude can be bounded in a single trajectory constraint through the inequality

$$-\infty \leq \min(C_g, C_h) \leq 0 \tag{54}$$

where

$$C_\mathrm{g} = \|\mathrm{S}_\mathrm{g} \mathbf{r}(t) - \mathbf{b}_\mathrm{g}\| + \mathbf{c}_\mathrm{g}^T \mathbf{r}(t) + a_\mathrm{g} \tag{55}$$

$$C_\mathrm{h} = \|\mathrm{S}_\mathrm{h} \mathbf{r}(t)\| + a_\mathrm{g} \tag{56}$$

Path constraints need to be satisfied at every time instant during the

landing. Pseudospectral techniques allow us to evaluate them discretely at Chebyshev-Gauss-Lobatto points.

Also in this case, the additional constraint on final mass of Eq. (26) is required:

$$m_{\text{dry}} \leq m(t_{\text{f}}) \leq m_0 \tag{57}$$

4.4. Optimization Problem

The generic optimization problem (2) for asteroidal landing is now expressed as:

Find T_0, t_{tof}, and η_0, in the domain defined by the inequalities (40), (42), and (43), that minimize fuel consumption computed by the Eq. (6), subject to constraints (44), (54), and (57).

The same NLP solver mentioned in Sec. 3.4 has been adopted for the solution of this optimization problem in all the simulations presented in this work.

5. Test Cases

An intensive test campaign has been conducted to assess the algorithm effectiveness in both the aforementioned scenarios. Results are presented in this section.

5.1. Test Procedure

The performances of the guidance algorithm are assessed thought Monte Carlo (MC) simulations with variable number of samples M. The guidance algorithm is written in Matlab® code, and tested on a Intel® Core™ i7-2630QM CPU at 2 GHz of frequency.

For both the scenarios, the test procedure is organized as follows. First, if required (dependently on the specific formulation), the tuning of the algorithm internal parameters is studied. Then, computational performances and divert capabilities are estimated by means of a first series of MC simulations, in which the guidance is run as standalone. Finally, ore or more MC simulations of a complete, realistic landing maneuver are presented. In these simulations the proposed guidance is applied to a lander model which includes realistic dynamics, a control logic, pulsed actuators and errors in both actuation and measurements. The enforcement of the additional constraints is verified, while possible sources of inaccuracies at touchdown are studied.

5.2. Planetary Landing Application Test

In order to make realistic assumptions on spacecraft architecture, the *ESA Lunar Lander* mission is taken as reference. Originally planned for launch in 2018 and designed for landing near the Moon's south pole, the mission's primary objectives include the demonstration of safe precision landing technology as part of preparations for participation to future human exploration of the Moon (Fisackerly et al., 2011). Recently, the project was put on hold at the 2012 ESA Ministerial Council, but the technology developed in the context of Lunar Lander phase B1 could be exploited for future cooperations in the area of Lunar Exploration with Russia. The Luna-Resource Lander mission, planned by Roscosmos for 2017, could be a testing platform for European precision landing technology, with the proposed Hazard Detection and Avoidance Experiment and the Visual Absolute/Relative Terrain Navigation Experiment (VNE) (Gardini, 2013).

The powered descend is assumed divided in 3 different phases (Hobbs et al., 2010):

- *Main Brake.* In this phase, starting from 15 km of altitude at the perilune of a transfer orbit, the thrust is constant at maximum value, and most of the orbital velocity is dropped. At the end of this phase, the spacecraft begins a pitch maneuver and the hazard detection system starts to work.

- *Approach.* At 2000 m of altitude, the thrust is reduced to get maneuverability. In this phase the thrust is variable and retargeting can be commanded.

- *Terminal Descent.* Once reached the vertical onto the TLS, at 30 m altitude, the lander performs a vertical descent at the constant speed of $1.5\,\mathrm{m\,s^{-1}}$ until touchdown.

Only the approach phase is the focus of this work. Assumptions on lander architecture are summarized in Table 1, and linear variation of inertia with respect to mass is assumed.

5.2.1. Algorithm Tuning and Performance Estimation

The polynomial formulation of the landing trajectory produces inherently exact states at the maneuver end. On the other hand, pseudospectal methods are used to carry out the integral of Eq. (6), necessary for mass computation.

Table 1: Lunar landing simulation: lander architecture assumptions.

Feature	**Value**	**UoM**
Wet mass m_{wet}	1500	kg
Wet matrix of inertia	$\text{diag}(1650, 1500, 1500)$	kg m^2
Dry mass m_{dry}	790	kg
Dry matrix of inertia	$\text{diag}(845, 675, 675)$	kg m^2
I_{sp}	325	s
I_{max}	1000	kg m^2
T_{min}	1000	N
T_{max}	2320	N
M_{Cmax}	40	N m

These methods involve the selection of an order of approximation N (the number of discrete point at which the approximated function is evaluated) which affects both precision and computational speed of the algorithm: higher degree improves the precision of the path evaluation, but slows the computation (by increasing the calculation time of single iterations).

The computational efficiency is assessed with a MC run with $M = 1 \times 10^5$ for values of $N = [10, 15, 20, 25, 30]$. In this simulation only the retargeting is considered, and the subsequent simulation of the diversion maneuver is not included. The retargeting is assumed to be ordered from the nominal landing path, at a random altitude between 500 m and 2000 m, with a random ordered diversion between -2000 m and $+2000$ m, independently in both downrange and crossrange directions. Figure 8 shows that the computation time is very stable, with very low dispersion.

The estimation of the algorithm precision is slightly different. The control profile calculated by the algorithm, reconstructed with Eqs. (17) and (9), is applied to the system (10) and integrated trough a traditional Runge-Kutta (4,5) method. The result is compared to the desired one to obtain the error on final position and speed. For each value of N, a set of 10 000 feasible points are considered. The initial altitude is constant at 2000 m, in order to maximize dispersion due to the approximation of the guidance profile reconstruction. The commanded diversion is random between -2000 m and $+2000$ m in both the horizontal directions. Resulting errors for position at landing are shown in Fig. 9. The polynomial approximation imposes on the

Table 2: Guidance algorithm preliminary performance assessment simulation: initial conditions for MC analysis.

Condition	**Nominal value**	**UoM**
Initial mass m_0	865	kg
Initial position $\mathbf{r}_0$	$[2000 \ -1060 \ 0]^T$	m
Initial speed $\mathbf{v}_0$	$[-35 \ 30 \ 0]^T$	$\mathrm{m\,s^{-1}}$
Initial pitch angle θ_0	-55	deg
Initial yaw angle ψ_0	0	deg

trajectory a smooth profile, on which the pseudospectral approximation is very effective. The error is small, and it can considered negligible from $N = 20$ onward. Then, 20 has been taken as nominal value for N.

A MC simulation is exploited also to assess the algorithm performances in terms of attainable landing area and fuel consumption. A series of 1×10^5 random diversions between ± 4000 m along both the horizontal axes is ordered at an altitude of 2000 m from a nominal trajectory. Initial conditions are summarized in Table 2. The attainable landing area can be obtained by correlating optimization results together with the coordinates of the TLSs, as shown by Fig. 10, in which only the points classified as feasible (satisfying all the constraints) by the optimization algorithm are shown. The system is able to compute a feasible landing path in an approximately circular landing area of radius larger than 2500 m centered at the nominal landing site (at the origin of the figure), a performance better than what is required for similar scenarios (Delaune et al., 2010; Johnson, 2006).

5.2.2. Objective Function and Constraints Functions

A planetary landing maneuver requires the optimization of only two parameters: is then easy to visualize graphically the objective and the constraint functions. Due to the polynomial formulation, the objective function maintains a very smooth shape, easy to be handled by NLP solvers. Figure 11 reports a typical example. The initial conditions are the same reported in Table 2, except for the initial position that is $\mathbf{r}_0 = [2000 \ -562.3 \ 1000]^T$ m. The function is mainly dependent on time-of-flight, while the dependency on the initial thrust magnitude is limited. In Fig. 12 the different infeasible regions associated to each nonlinear constraint are shown, and the solution found is compared to the actual global optimum (computed solving the opti-

mization problem with the nonlinear programming solver SNOPT). Note that the absence of local minima together with a compact, although non-convex, feasibility region produces an easy-to-solve optimization problem. With a simple compass method we quickly compute a solution that is only 5.64% higher than the actual (parameterized) optimum. Note that similar considerations apply to all the simulations presented in this paper.

5.2.3. Comparison to True Optimal Maneuver

The adopted polynomial form actually limits the shape that the trajectory can assume. Then, the optimal parameterized solution generally differs with respect to the true optimal, which is known to have a bang-bang solution (Topcu et al., 2005). In order to estimate the distance from the optimum, the proposed algorithm is compared with an open-loop numerical solution, computed through a pseudospectral collocation method (using Tomlab/PROPT® optimization software). Figure 13 refers to the same case adopted in Fig. 11 and Fig. 12. The solution found by the semi-analytical guidance optimized with the modified compass search method is labeled "SAGuid (MCS)"; also the true optimal parameterized solution is included (labeled "SAGuid (optimal)"), computed by optimizing the semi-analytical guidance with SNOPT. Thrust, attitude, and mass profiles are showed. The correlation between the time-of-flight and the optimality of the solution, together with the discontinuous structure of the true optimal thrust profile are clearly visible. Also, it can be seen as polynomial solutions are approximations of the true optimal. In this specific case, the solution found by the proposed approach requires a fuel consumption 11% higher than the optimal one. As the requested diversion decrease, modified compass search performances improve: in Fig. 14 the same optimality comparison for a nominal approach phase (see Table 2) is shown. In this case the solution is much closer to the optimal one and it differs in terms of propellant by only 3.97%.

5.2.4. Landing Simulation: Nominal Navigation Errors

The guidance algorithm is tested in a 7DoF (three-dimensional rototranslation with variable mass) retargeting simulator of a lunar landing, realized in Matlab® and Simulink® environment.

It is supposed that a nominal trajectory is known, obtained through traditional optimization methods as in Lunghi et al. (2013). The simulation covers the approach phase from 2000 m altitude to the beginning of the terminal descent onto the TLS, over a timespan of the order of magnitude

Table 3: Complete lunar landing simulation: initial and final conditions for MC analysis.

Condition	**Nominal value**	$\mathbf{1\sigma}$	**UoM**
Initial mass m_0	865	± 10	kg
Initial position $\mathbf{r}_0$	$[2000 \ -1060 \ 0]^T$	$\pm[30 \ 600 \ 600]^T$	m
Initial speed $\mathbf{v}_0$	$[-35 \ 30 \ 0]^T$	$\pm[0.5 \ 0.5 \ 0.5]^T$	$\mathrm{m\,s^{-1}}$
Initial pitch angle θ_0	-55	± 5	deg
Initial yaw angle ψ_0	0	± 5	deg
Target position $\mathbf{r}_\mathrm{f}$	$[30 \ 0 \ 0]^T$	-	m
Target speed $\mathbf{v}_\mathrm{f}$	$[-1.5 \ 0 \ 0]^T$	-	$\mathrm{m\,s^{-1}}$
Target pitch angle θ_f	-90	-	deg
Target yaw angle ψ_f	0	-	deg

of 70 s. In order to test both effectiveness and diversion capability of the algorithm, a MC simulation with $M = 1000$ is adopted. Table 3 shows initial and final boundary constraints imposed, together with dispersion added to initial conditions, to include uncertainties at the end of the main brake phase. Larger dispersions are considered for the horizontal components of the initial position. In fact, all the considered dynamics are relative, from the spacecraft with respect to the landing site. During trajectory computation, ordering a retargeting or shifting the initial position of the same magnitude toward the opposite direction are equivalent (actually, shifting the initial position is exactly what the guidance algorithm does). Thus, the introduction of larger dispersions in the horizontal components of the initial position allows us also to evaluate retargeting capabilities, including both position uncertainties and random ordered diversions.

The algorithm is tested in a landing scenario in which disturbances and navigation errors are most real as possible. A disturbance torque is introduced by a 10 mm thrust misalignment from the spacecraft center of mass. Errors in the states passed to the guidance block are considered to emulate a real navigation system. Attitude is supposed to be estimated by an Inertial Measurement Unit (IMU), whose performances are summarized in Table 4.

The presence of a vision-based navigation system is assumed to estimate position and speed. This kind of systems makes use of a radar or laser altimeter to estimate the altitude with which the images taken by cameras are resized to the proper scale. Since altimeters absolute error increases with the

Table 4: Lunar landing simulation: IMU performance properties.

Property	**Value**	**UoM**
Scale factor	1	ppm
Misalignment Error	170	µrad
Bias Error	0.005	deg/h
ARW noise density	0.005	deg/$\sqrt{\text{h}}$

distance from the ground, the error in the estimate is modeled as a Gaussian random error with zero mean and standard deviation varying linearly with the altitude. The values adopted as reference are $\pm 25\,\text{m}$ and $\pm 0.4\,\text{m}\,\text{s}^{-1}$ (1σ) at 2000 m altitude (they are both assumed to be null at zero altitude). The guidance subsystem recalculates the trajectory every 5 s, to cope with measure dispersion. From the guidance profile, at every update of the control system, target quaternions and angular velocities are computed, and a Proportional Integral Derivative controller is used to calculate theoretical control torques. The attitude is assumed to be controlled by a cluster of chemical thrusters able to supply a constant torque of $\pm 40\,\text{N}\,\text{m}$ on each axis. Theoretical control torques are processed by a Pulse Width Pulse Frequency (PWPF) modulator that commands thrusters firings. The considered guidance and control systems update rate is 20 Hz.

Figure 15 shows the obtained 3D trajectories. Dispersions in position and velocity, for their horizontal (Fig. 16) and vertical (Fig. 17) components are reported. Figure 18 shows the obtained final attitude distribution. Overall, the system attains a good performance despite of the uncertainties. The dimensions of the obtained 3σ ellipse are comparable to a possible lander footprint (Fisackerly et al., 2011), giving to the system hazard avoidance capabilities.

5.2.5. Landing Simulation: Sensitivity to Navigation Errors

Additional MC runs, with $M = 300$, are exploited to assess the sensitivity of the system to navigation errors. The same initial and target conditions of Table 3 are assumed, except for the value of the navigation errors standard deviation at the maneuver start. The following values are considered for position and velocity estimation:

- *Pessimistic Case* (PC): Position error: $\pm 45\,\mathrm{m}$; speed error: $\pm 0.4\,\mathrm{m\,s^{-1}}$ (1σ);
- *Optimistic Case* (OC): Position error: $\pm 10\,\mathrm{m}$; speed error: $\pm 0.4\,\mathrm{m\,s^{-1}}$ (1σ);
- *Exact Case* (EC): Ideal measures with no navigation errors.

As for the nominal case (presented in the previous section) navigation errors are supposed to decrease linearly with the altitude, and they are assumed to be null at touchdown. The EC is considered to highlight the effect of the navigation system over the final landing accuracy. Figure (19) shows a comparison of the results obtained for the 3 cases, including also the *Nominal Case* (NC) presented in section 5.2.4. The obtained 3σ dispersion ellipses for final horizontal position and velocity are presented. It can be seen that dispersion due to control system only is at least one order of magnitude lower than the one due to navigation. This proves that landing precision is mainly affected by navigation errors.

5.3. NEA Landing Application Test

A landing on the asteroid 1999 $\mathrm{RQ_{36}}$ "Bennu", target of the mission OSIRIS-REx, planned for launch by NASA in 2017 (Furfaro et al., 2013b), is selected as NEA application test. Table 5 summarizes the assumed asteroid nominal parameters.

The case of an equatorial landing is here presented. The spacecraft is supposed to start at a near hovering condition; the target state is on the vertical over the selected landing site, at 3 m of altitude, with a vertical speed of $0.1\,\mathrm{m\,s^{-1}}$ toward the ground and a null horizontal speed. Adopted parameters, initial and target states, common to all the simulations here presented, are summarized in Table 6.

5.3.1. Algorithm Performance Estimation

The assessment of the computational performance is performed through a MC simulation, with the same parameters of Table 6 and $M = 10000$. Figure 20 shows that the additional optimization variable causes an increase of the computation time up to one order of magnitude, compared to the planetary landing case. Anyway, due to the relatively large time-of-flight typical of maneuvers in low-gravity environment, it remains perfectly compatible with maneuver requirements.

Table 5: 1999 RQ_{36} "Bennu" nominal parameters.

Feature	**Value**	**UoM**
Major semi-axis, a	350	m
Intermediate semi-axis, b	287	m
Minor semi-axis, c	250	m
Density, ρ	1400	$\mathrm{kg\,m^{-3}}$
Rotational rate, ω	4.04×10^{-4}	$\mathrm{rad\,s^{-1}}$

Table 6: NEA landing: MC parameters, initial and target states.

Condition	**Nominal value**	$\mathbf{1\sigma}$	**UoM**
Initial Position, $\mathbf{r}_0$	$[1500, 0, 0]^T$	$\pm[50, 100, 100]^T$	m
Initial Velocity, $\mathbf{v}_0$	$[0, 0, 0]^T$	$\pm[0.1, 0.1, 0.1]^T$	$\mathrm{m\,s^{-1}}$
Initial Mass, m_0	750	-	kg
Target Position, $\mathbf{r}_\mathrm{f}$	$[0, 290, 0]^T$	-	m
Target Velocity, $\mathbf{v}_\mathrm{f}$	$[0, -0.1, 0]^T$	-	$\mathrm{m\,s^{-1}}$
Specific Impulse, I_sp	315	-	s
Max Available Thrust, T_max	10	-	N
Dry Mass, m_dry	740	-	kg
Asteroid Density, ρ	1400	$\pm 10\%$	$\mathrm{kg\,m^{-3}}$
Asteroid Rotational rate, ω	4.04×10^{-4}	$\pm 10\%$	$\mathrm{rad\,s^{-1}}$

The estimation of attainable landing area and fuel consumption is carried out considering the nominal initial conditions of Table 6. The landing site is varied over a regular grid of 1° resolution in both latitude and longitude. From Fig. 21 it is shown that the spacecraft can reach any site on the NEA surface, and that the fuel consumption presents an asymmetry in longitude, due to the asteroid rotational rate.

5.3.2. Landing Simulation: Exact Measures

Due to the weak gravitational acceleration involved, in a NEA landing case the theoretical thrust can assume very low values (also for long times) that could be not attainable by traditional propulsion systems. Thus, it is assumed that the thrust is supplied by the same system of chemical thrusters used by ACS, filtered by a PWPF modulation system.

Sharing of the propulsion system is made possible by the slow dynamics of both attitude and thrust control systems. During the landing maneuver, the spacecraft is simply required to point toward the asteroid center of mass. The actual Guidance, Navigation and Control (GNC) system architecture is represented in Fig. 22: the navigation system determines position $\mathbf{r}$, velocity $\mathbf{v}$, attitude quaternions $\mathbf{q}$ and rotational rate vector $\boldsymbol{\omega}$. Attitude control system computes the control torques $\mathbf{M}_c$, while the adaptive guidance system provides the control thrust vector $\mathbf{T}_c$. Their actuation is fused together by PWPF modulation in a unique thruster activation scheme. This configuration presents several advantages:

- The 3 components of the thrust vector can be generated independently, in body axes, leaving the spacecraft free to assume any attitude imposed by vision-based navigation system.
- There is no need of additional dedicated devices devoted to low-thrust.
- No additional constraints are imposed over high-trust propulsion system (devoted to large scale orbital control), in terms of thrust throttleability or minimum thrust level.

As a result of this architecture, attitude and propulsion are assumed as independent and the simulation is reduced to 4 degrees of freedom (3 translations and the variable mass). As the landing site gets closer, the trajectory is updated by additional runs of the algorithm, performed at 1000, 500, 300, 200 and 150 m from the target. In this way, dispersion due to

modulation is compensated. In this article an example of equatorial landing is reported: asteroid and lander data, together with initial conditions, TLS, and their relative dispersions, are the same reported in Tables 5 and 6. MC simulations with $M = 300$ are run.

As visible from Fig. 23-25, the modulation of the thrust introduces a certain error in the attained position over the landing site. Anyway this error remains into acceptable limits, with an obtained final maximum accuracy of 8 m (3σ) from the target.

5.3.3. Landing Simulation: Navigation Errors

In the GNC system schematic represented in Fig. 22, is possible to see how navigation errors influence trajectory calculation. At the time the trajectory is recomputed, errors in position and velocity determination affects directly the obtained path. Moreover, since the thrust profile obtained from the optimization is expressed in asteroid reference frame, a conversion in spacecraft body-fixed frame is required at every control timestep to properly command the actuators. Errors in attitude determination affect the direction of the actual thrust, introducing additional errors in attained states at the maneuver's end.

Assuming the presence of a visual-based navigation system, errors in position and velocity are modeled as Gaussian errors, with zero mean and variable standard deviation proportional to the distance between the asteroid and the spacecraft. The values of 25 m and 0.1 m s^{-1}, at the reference distance of 2000 m are adopted (they are both considered null on the surface of the asteroid). The presence of a star tracker is considered for attitude determination. The attitude error is considered as Gaussian with a bias (mean) rotation of 5 arcsec and a standard deviation of 3 arcsec around each axis. As in the previous case, dispersion at touchdown is limited by updating the trajectory as the spacecraft gets closer to the target, at the same target distances of the first simulation. An MC run with $M = 300$ is carried out.

Due to the relative long time requested by the maneuver, together with the applied open-loop control, errors in states determination at the retargeting epoch propagate up to potentially unacceptable values, especially for position (while a good precision in velocity is preserved), as shown in Fig. 26 and 27. In particular, the error obtained in final position is almost of the same order of magnitude of the asteroid's size itself, and cannot be accepted.

5.3.4. Landing Simulation: Waypoint Trajectory

As possible method to regain precision at landing, the introduction of a waypoint along the trajectory is investigated. The trajectory computation is split into two concatenate maneuvers: in the first one, the target of the trajectory optimization is not the TLS, but the point 250 m above it, along the local vertical direction. Once this first maneuver is ended, the system performs a second optimization toward the final target. A third MC with $M = 300$ is adopted.

A level of precision of the same order of magnitude of the of the case without navigation errors is recovered, as visible by comparing Fig. 28 – 30 with the correspondent Fig. 23 – 25. This result is achieved without a significant impact on propellant consumption as shown in Fig. 31.

6. Conclusion

The purpose of this work was the development of a retargeting algorithm for spacecraft landing, capable of updating and correcting a landing trajectory almost to the touchdown.

A novel approach based on the inclusion of free parameters in a classical polynomial formulation is proposed, in order to improve flexibility in the landing site choice, and to consider additional non linear constraints during the descent, such as thrust magnitude and attitude control torques boundaries. The resulting algorithm has light computational load, and maintains a high divert capability even with the use of a simple optimization algorithm.

The flexibility and the robustness of the proposed approach have been tested by applying it in retargeting simulations of two very different cases, a lunar landing and a landing over a NEA, characterized by time scales and dynamics separated by at least 2 orders of magnitude. Monte Carlo simulations have been exploited to assess the algorithm retargeting capabilities.

The enforcement of the additional constraints has been verified by complete landing MC simulations. The proposed guidance has been applied to a lander simulator, including perturbed states (introduced in order to emulate navigation system errors), a simple control system, and pulsed actuators. The guidance algorithm resulted able to find a feasible landing trajectory in all the tested cases, with attainable landing areas larger than what is expected to be required in future missions.

It has been observed that accuracy at touchdown is mainly affected by navigation errors. Their impact can be mitigated by updating the landing

trajectory several times during the descent. This strategy has proved effective especially in fast maneuvers, as in the tested lunar landing case. On the other hand, it has been observed that in the case of slow maneuvers (as in the NEA landing simulation) errors can propagate more easily. Introducing an opportune waypoint on the landing trajectory, a high level of precision is recovered, with a negligible effect on fuel consumption. In these situations an accurate project of the retargeting phase and of the guidance logic (waypoints, update frequency, open or close loop control between two consecutive updates) is required.

Appendix: Modified Compass Search Method

The optimization problems presented in this paper can be solved through many different algorithms. Fast computation must be privileged, in perspective of a real-time implementation for on-board hardware. In this context, derivative-free optimization methods are attractive, because they don't require any differentiation of the cost function, treating it as a "black-box".

The *Compass Search Method* has been adopted as optimizer for all the simulations presented in this paper. Since this simple method is suitable only for unconstrained problems, some modifications have been introduced to handle also non linear constraints. Only the modifications applied to constraints handling are here described. For a detailed description of the classical compass search method, see (Kolda et al., 2003).

First, the optimization variables are normalized, to give them the same relative weight in the optimization:

$$\tilde{\mathbf{x}} = \frac{\mathbf{x} - \mathbf{x}_L}{\mathbf{x}_U - \mathbf{x}_L} \quad \Leftrightarrow \quad \mathbf{x} = \tilde{\mathbf{x}}(\mathbf{x}_U - \mathbf{x}_L) + \mathbf{x}_L \tag{58}$$

Normalized optimization variables can vary between 0 and 1. Then, a feasibility function $F(\tilde{\mathbf{x}})$ is created, defined as

$$F(\tilde{\mathbf{x}}) = \sum_{j=0}^{N_C} \frac{1}{w_{\mathrm{F}j}} \max(0, \tilde{c}_j) \tag{59}$$

where $\tilde{c}_j$ are the components of a generalized constraints vector $\tilde{\mathbf{c}}(\tilde{\mathbf{x}})$, and $\mathbf{w}_\mathrm{F}$ is a vector of weights, that normalize different constraints that can have

different orders of magnitude:

$$\tilde{\mathbf{c}}(\tilde{\mathbf{x}}) = \begin{bmatrix} \mathbf{c}_L - \mathbf{c}(\tilde{\mathbf{x}}) \\ \mathbf{c}(\tilde{\mathbf{x}}) - \mathbf{c}_U \\ 0 - \tilde{\mathbf{x}} \\ \tilde{\mathbf{x}} - 1 \end{bmatrix}, \quad \mathbf{w}_{\mathrm{F}} = \begin{bmatrix} \mathbf{c}_U - \mathbf{c}_L \\ \mathbf{c}_U - \mathbf{c}_L \\ \mathbf{x}_U - \mathbf{x}_L \\ \mathbf{x}_U - \mathbf{x}_L \end{bmatrix} \tag{60}$$

The glide-slope lower bound of Eqs. (23,45), and consequently the corresponding weight, is infinite. An improper constraint evaluation is avoided by setting this weight to a value with the correct order of magnitude. $r_{\mathrm{x}}(t_0)$ and $h_{\min}$ are adopted, respectively for the planetary and the NEA landing cases. A feasible set of optimization variables $\tilde{\mathbf{x}}$ corresponds to a null value of the feasibility function. On the contrary, in case of infeasibility, $F(\tilde{\mathbf{x}}) > 0$.

The optimization algorithm operates in two phases. Firstly, an unconstrained compass search on the function $F(\tilde{\mathbf{x}})$ is performed. The search is stopped when a feasible point is found ($F(\tilde{\mathbf{x}}) = 0$), or when the iteration limit is reached. In this case, the problem is classified as infeasible. If the fist step is successful the algorithm keeps solving for the optimum through an unconstrained search on the modified cost function $\Phi(\tilde{\mathbf{x}})$, defined as

$$\Phi(\tilde{\mathbf{x}}) = f(\tilde{\mathbf{x}}) + \xi \operatorname{sgn}\big(F(\tilde{\mathbf{x}})\big) \tag{61}$$

where $f(\tilde{\mathbf{x}})$ is the original cost function of the problem (2), and ξ is a number certainly greater than the maximum value that cost function can assume.

References

Açikmeşe, B., Ploen, S. R., 2007. Convex programming approach to powered descent guidance for Mars landing. Journal of Guidance, Control and Dynamics 30 (5), 1353–1366.

Berry, K., Sutter, B., May, A., Williams, K., Barbee, B., Beckman, M., Williams, B., 2013. OSIRIS-REx touch-and-go (TAG) mission design and analysis. Advances in the Astronautical Sciences 149, 667–678.

Betts, J. T., 1998. Survey of numerical methods for trajectory optimization. Journal of Guidance, Control, and Dynamics 21 (2), 193–207.

Blackmore, L., Açikmeşe, B., Scharf, P., 2010. Minimum-landing-error

powered-descent guidance for mars landing using convex optimization. Journal of Guidance, Control and Dynamics 33 (4), 1161–1171.

Canuto, C., Hussaini, M. Y., Quarteroni, A., Zang, T. A., 1988. Spectral methods in fluid dynamics. Springer, New York.

Carpenter, J. D., Fisackerly, R., De Rosa, D., Houdou, B., 2012. Scientific preparations for lunar exploration with the European Lunar Lander. Planetary and Space Science 74 (1), 208–223.

Cheng, A. F., 18–22 March 2013. AIDA: Test of asteroid deflection by spacecraft impact. In: 44th Lunar and Planetary Science Conference. The Woodlands, TX.

Condon, G. L., Williams, J., 5–9 May 2014. Asteroid Redirect crewed mission nominal design and performance. In: SpaceOps Conference. Pasadena, CA.

Delaune, J., De Rosa, D., Hobbs, S., 2–5 August 2010. Guidance and control system design for lunar descent and landing. In: AIAA Guidance, Navigation, and Control Conference. Toronto, Ontario Canada.

Fahroo, F., Ross, I. M., 2002. Direct trajectory optimization by a Chebyshev pseudospectral method. Journal of Guidance, Control and Dynamics 25 (1), 160–166.

Fisackerly, R., Pradier, A., Gardini, B., Houdou, B., Philippe, C., De Rosa, D., Carpenter, J., 27–29 September 2011. The ESA Lunar Lander mission. In: AIAA SPACE Conference and Exposition. Long Beach, CA.

Flandin, G., Polle, B., Despré, N., Lheritier, J., Perrimon, N., Blanc-Paques, P., 2–5 August 2010. Maturing vision based navigation solutions to space exploration. In: AIAA Guidance, Navigation, and Control Conference. Toronto, Ontario Canada.

Furfaro, R., Cersosimo, D., Wibben, D., 2013a. Asteroid precision landing via multiple sliding surfaces guidance techniques. Journal of Guidance, Control, and Dynamics 36 (4), 1075–1092.

Furfaro, R., Gaudet, B., Wibben, D. R., Simo, J., 19–22 August 2013b. Development of non-linear guidance algorithms for asteroids close-proximity operations. In: AIAA Guidance, Navigation, and Control Conference. Boston, MA.

Gal-Edd, J., Cheuvront, A., 5–9 May 2014. The OSIRIS-REx asteroid sample return: Mission operations design. In: SpaceOps Conference. Pasadena, CA.

Gardini, B., 18–19 February 2013. OUTLOOK after the CM 2012. In: European Commission Workshop on Space Science and Exploration. Madrid, Spain.

Gerth, I., Mooij, E., 13–17 January 2014. Guidance for autonomous precision landing on atmosphereless bodies. In: AIAA Guidance, Navigation, and Control Conference. National Harbor, MD.

Geurts, K., Fantinati, C., Ulamec, S., Willnecker, R., 5–9 May 2014. Rosetta lander: On-comet operations preparation and planning. In: SpaceOps Conference. Pasadena, CA.

Hawkins, M., Guo, Y., Wie, B., 13–16 August 2012. ZEM/ZEV feedback guidance application to fuel-efficient orbital maneuvers around an irregular-shaped asteroid. In: AIAA Guidance, Navigation, and Control Conference. Minneapolis, MN.

Hobbs, S., Rosa, D., Delaune, J., 2–5 August 2010. Guidance and control system design for lunar descent and landing. In: AIAA Guidance, Navigation, and Control Conference. Toronto, Ontario Canada.

Johnson, M. C., 21–24 August 2006. A parameterized approach to the design of lunar lander attitude controllers. In: AIAA Guidance, Navigation, and Control Conference. Keystone, CO.

Klumpp, A. R., 1974. Apollo lunar descent guidance. Automatica 10 (2), 133–146.

Kolda, T., Lewis, R., Torczon, V., 2003. Optimization by direct search: New perspectives on some classical and modern methods. SIAM Review 45 (3), 385–482.

Lara, M., Scheeres, D., 2002. Stability bounds for three-dimensional motion close to asteroids. Journal of the Astronautical Sciences 50 (4), 389–409.

Lunghi, P., Lavagna, M., Armellin, R., 23–27 September 2013. Adaptive semi-analytical guidance for autonomous planetary landing. In: 64th International Astronautical Congress. Beijing, China.

Marshall, P. F., Norris, S. D., 10–12 September 2013. Orion project status. In: AIAA SPACE Conference and Exposition. Madrid, Spain.

Michel, P., Barucci, M. A., Cheng, A. F., Böhnhardt, H., Brucato, J. R., Dotto, E., Ehrenfreund, P., Franchi, I. A., Green, S. F., Lara, L.-M., Marty, B., Koschny, D., Agnolon, D., 2014. MarcoPolo-R: Near-earth asteroid sample return mission selected for the assessment study phase of the ESA program cosmic vision. Acta Astronautica 93 (0), 530–538.

Riedel, J., Vaughan, A., Werner, R. A., Tseng-Chan, W., Nolet, S., Myers, D., Mastrodemos, N., Lee, A., Grasso, C., Ely, T., Bayard, D., 2–5 August 2010. Optical navigation plan and strategy for the lunar lander Altair; OpNav for lunar and other crewed and robotic exploration applications. In: AIAA Guidance, Navigation, and Control Conference. Toronto, Ontario Canada.

Scheeres, D. J., 1994. Dynamics about uniformly rotating triaxial ellipsoids: Applications to asteroids. Icarus 110 (2), 225–238.

Topcu, U., Casoliva, J., Mease, K., 15–18 August 2005. Fuel efficient powered descent guidance for Mars landing. In: AIAA Guidance, Navigation, and Control Conference and Exhibit. San Francisco, CA.

Werner, R., Scheeres, D., 1996. Exterior gravitation of a polyhedron derived and compared with harmonic and mascon gravitation representations of asteroid 4769 Castalia. Celestial Mechanics and Dynamical Astronomy 65 (3), 313–334.

Wong, E., Masciarelli, J., Singh, G., 5–8 August 2002. Autonomous guidance and control design for hazard avoidance and safe landing on Mars. In: AIAA Atmospheric Flight Mechanics Conference and Exhibit. Monterey, CA.

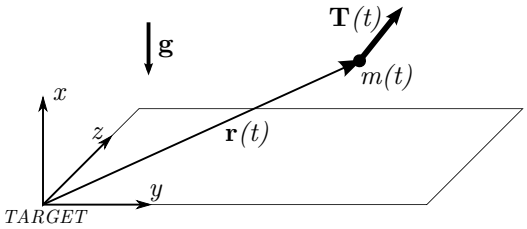

Figure 1: Ground reference system.

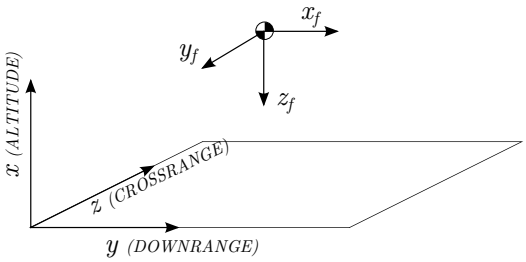

Figure 2: Flight reference system.

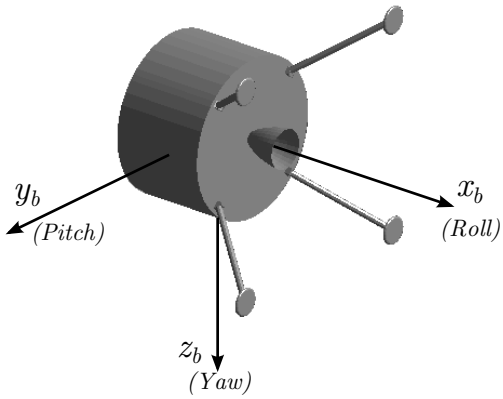

Figure 3: Body-fixed reference system.

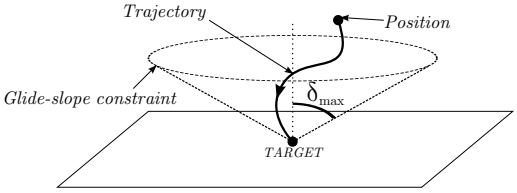

Figure 4: Glide-slope constraint.

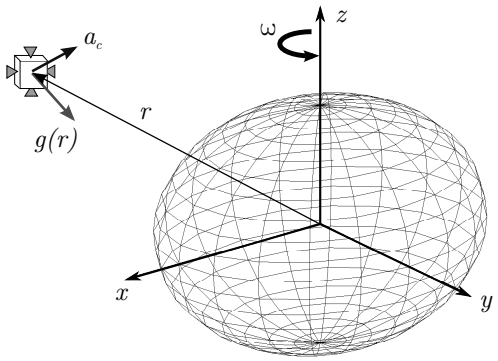

Figure 5: Body-fixed asteroid reference frame.

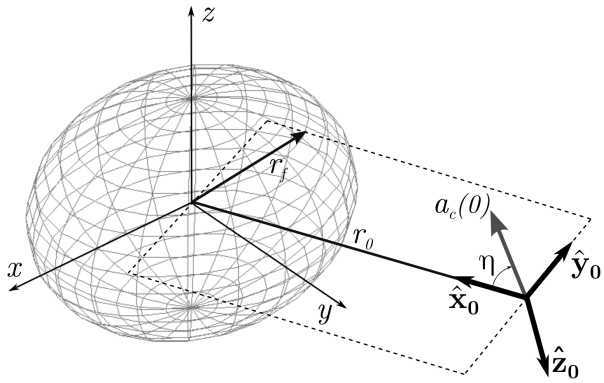

Figure 6: Initial control acceleration.

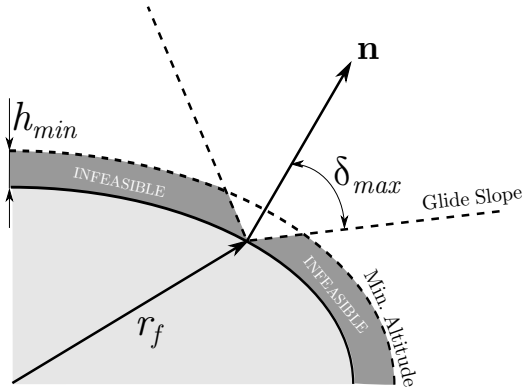

Figure 7: Glide-slope and minimum altitude constraints.

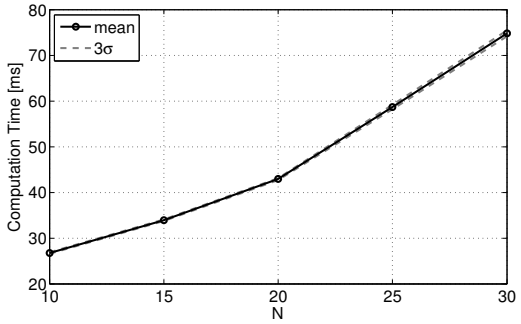

Figure 8: Lunar landing: computational time as a function of approximation order N.

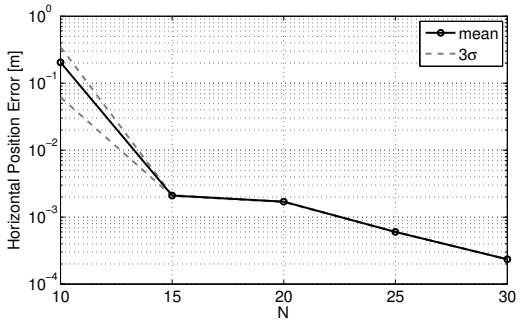

Figure 9: Lunar landing: position error at landing as a function of approximation order N.

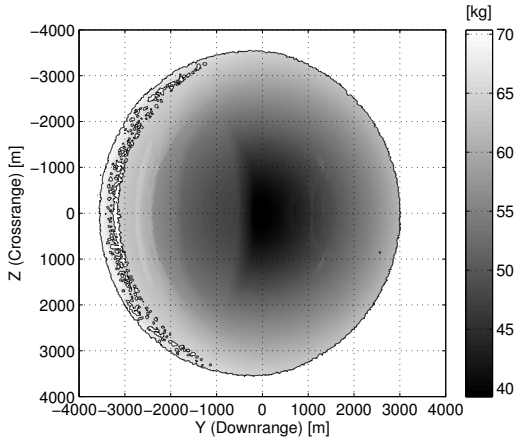

Figure 10: Lunar landing: attainable area and fuel consumption, diversion ordered from 2000 m altitude, from a nominal landing path.

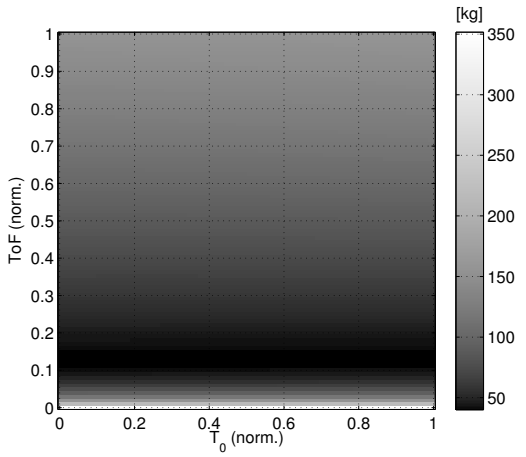

Figure 11: Lunar landing: objective function example.

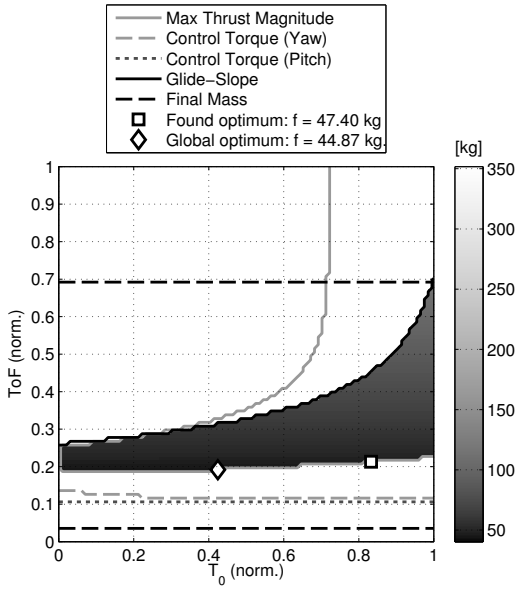

Figure 12: Lunar landing: nonlinear constraints and solution found example . The solution found is 5.64% far than global optimum.

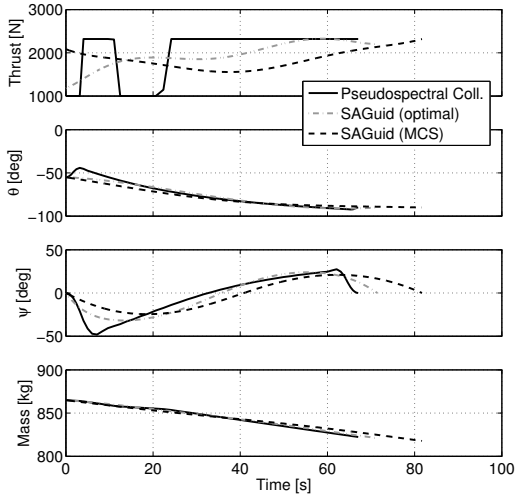

Figure 13: Lunar landing: comparison to true optimal solution example, retargeting maneuver. Polynomial solutions approximate the true optimal. The propellant consumption found by Modified Compass Search is 11% higher than the solution computed by pseudospectral collocation.

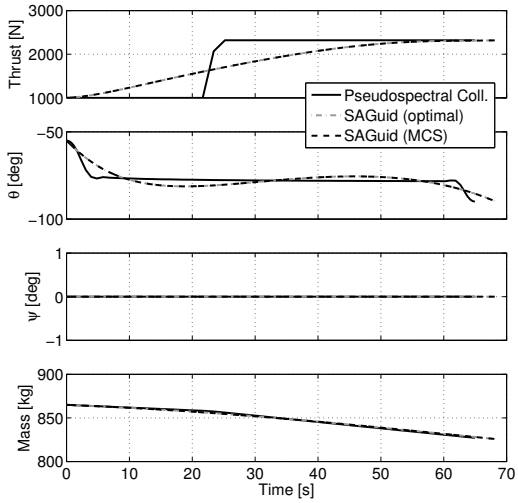

Figure 14: Lunar landing: comparison to true optimal solution example, nominal landing. The propellant consumption found by Modified Compass Search corresponds to the true optimal parameterized solution, 3.97% higher than the true optimal.

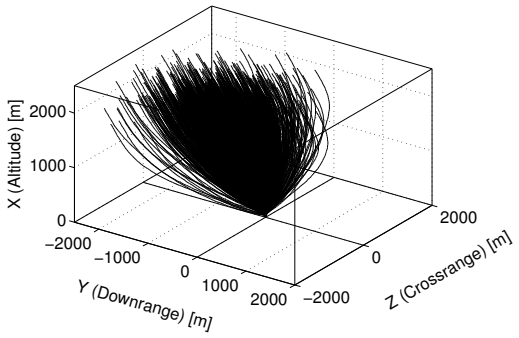

Figure 15: Lunar landing MC simulation ($M = 1000$): 3D Landing trajectories.

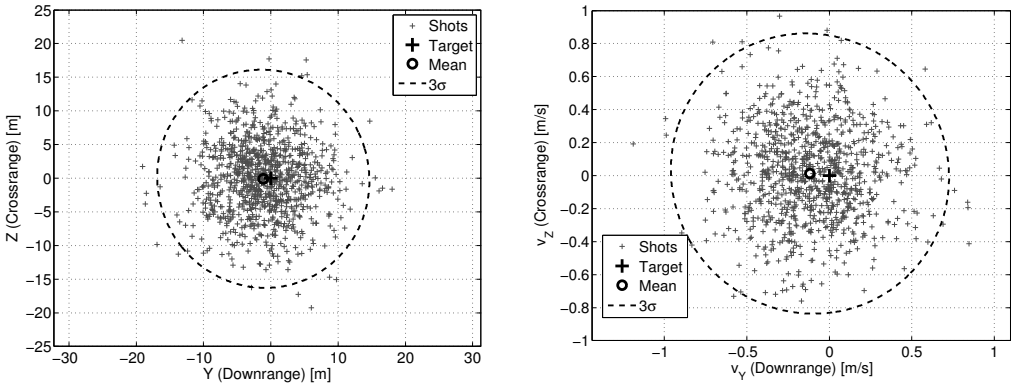

(a) Position. (b) Horizontal velocity.

Figure 16: Lunar landing MC simulation: dispersion in final position and velocity, horizontal components.

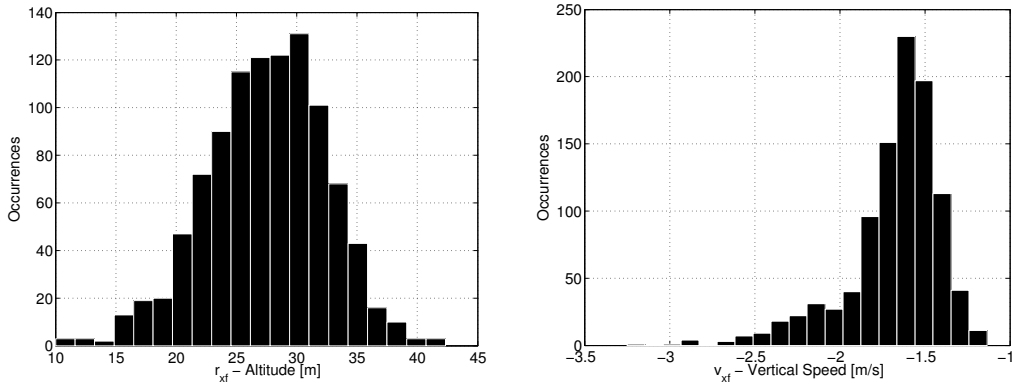

(a) Final altitude. (b) Final vertical speed.

Figure 17: Lunar landing MC simulation: dispersion in final position and velocity, vertical components.

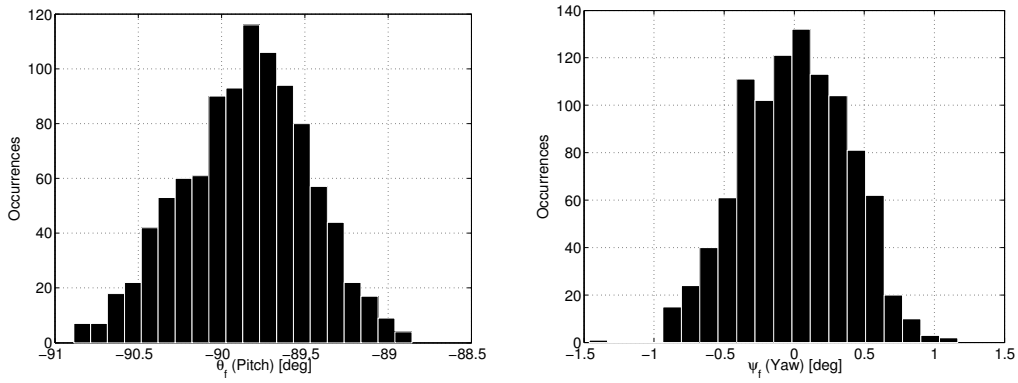

(a) Pitch angle. (b) Yaw angle.

Figure 18: Lunar landing MC simulation: final attitude dispersion.

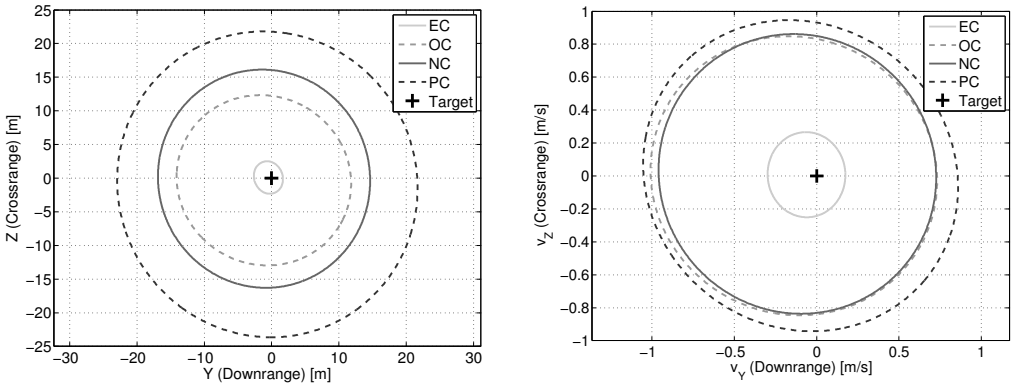

(a) Position. (b) Velocity.

Figure 19: Lunar landing MC simulation: navigation errors effect. 3σ dispersion ellipses at touchdown for position (a) and velocity (b).

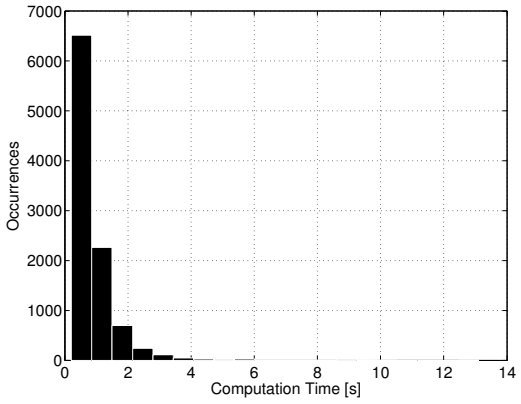

Figure 20: NEA landing: algorithm computation time.

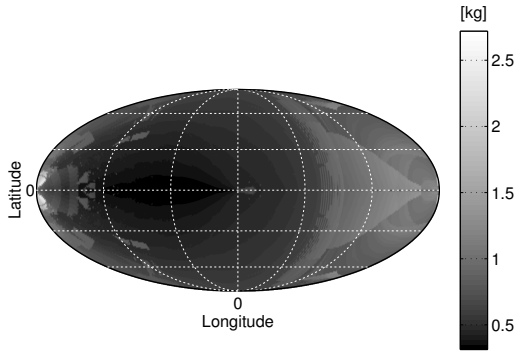

Figure 21: NEA landing: attainable area and fuel consumption.

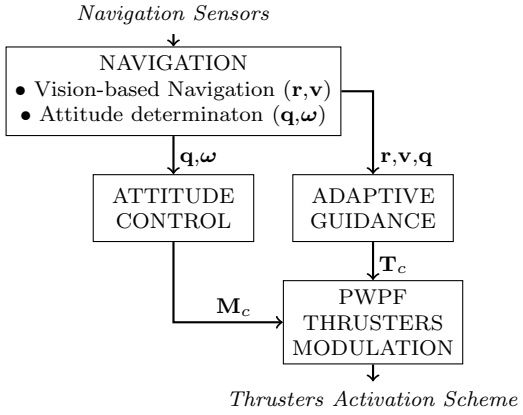

Figure 22: NEA landing: logical schematic of the GNC System.

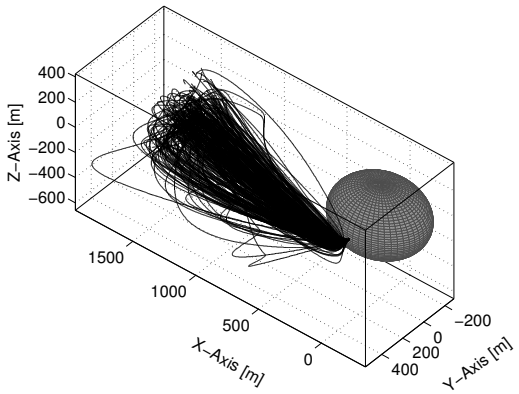

Figure 23: NEA landing MC simulation ($M = 300$), no navigation errors: 3D landing trajectories.

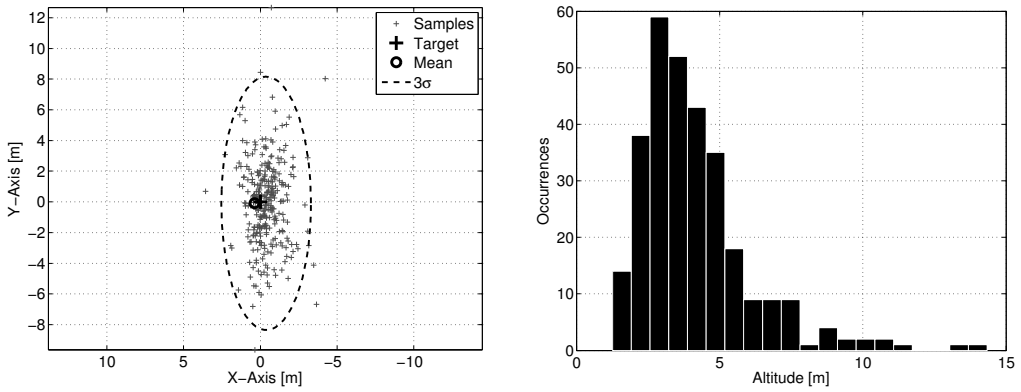

(a) Horizontal components.

(b) Altitude.

Figure 24: NEA landing MC simulation, no navigation errors: final position distribution.

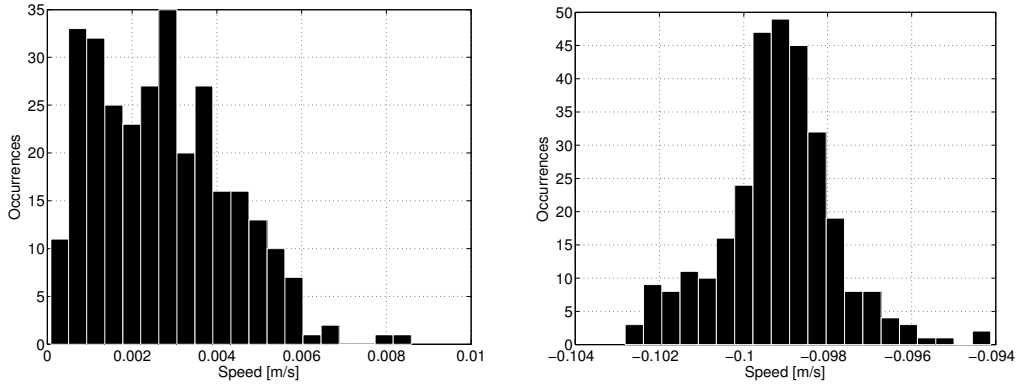

(a) Horizontal components. (b) Vertical component.

Figure 25: NEA landing MC simulation, no navigation errors: final velocity distribution.

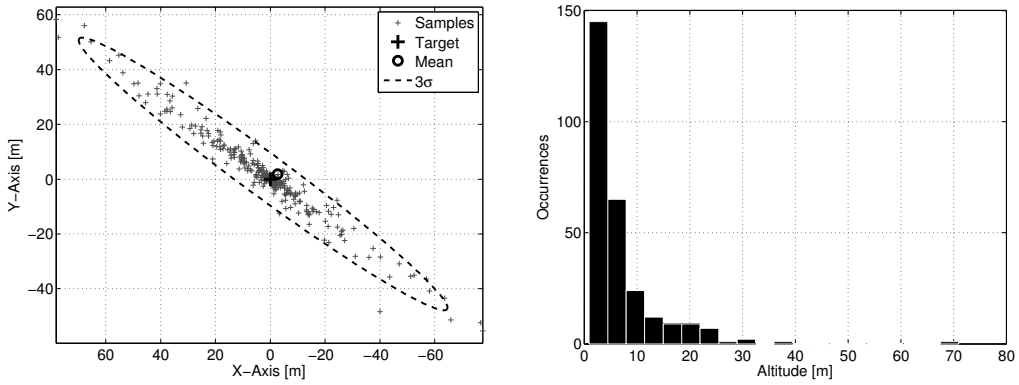

(a) Horizontal components. (b) Altitude.

Figure 26: NEA landing MC simulation ($M = 300$), navigation errors effect: final position distribution.

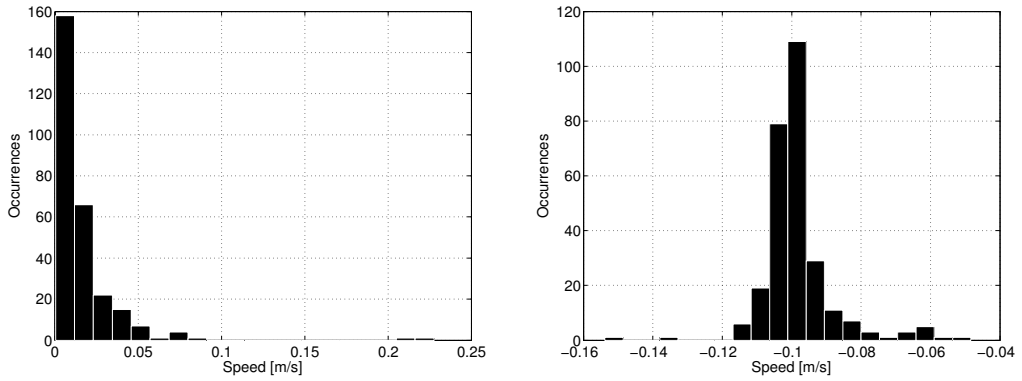

(a) Horizontal components. (b) Vertical component.

Figure 27: NEA landing MC simulation, navigation errors effect: final velocity distribution.

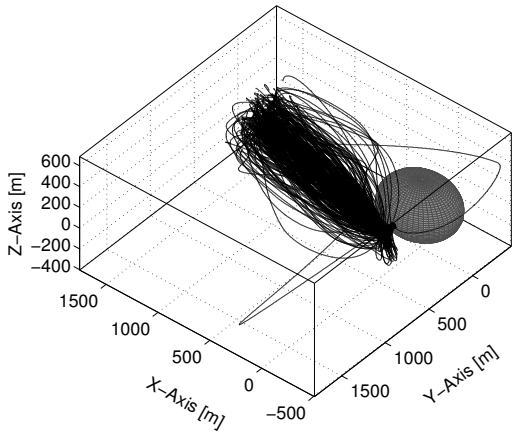

Figure 28: NEA landing MC simulation ($M = 300$), waypoint improved maneuver case: 3D landing trajectories.

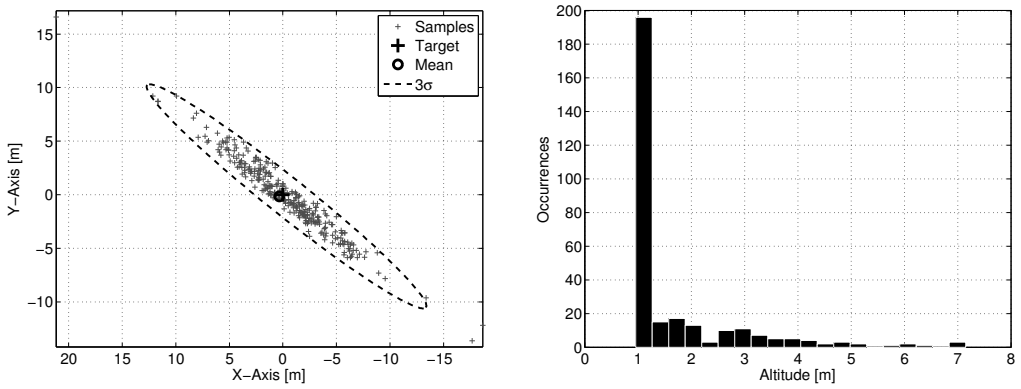

(a) Horizontal components. (b) Altitude.

Figure 29: NEA landing MC simulation, waypoint improved maneuver case: final position distribution.

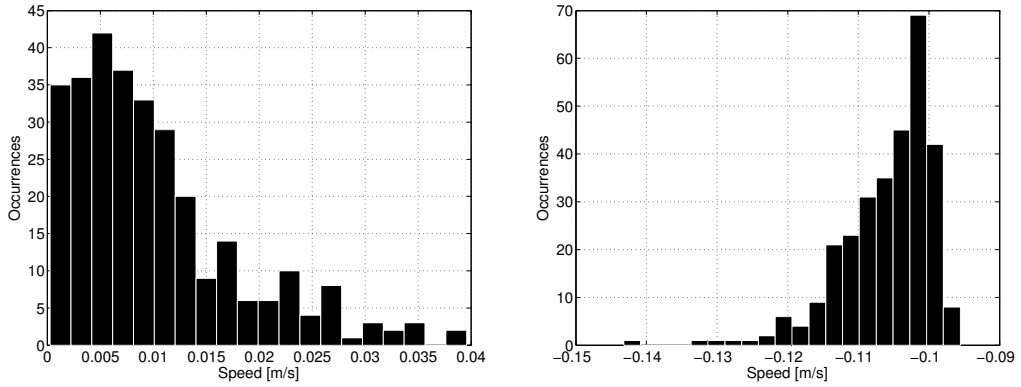

(a) Horizontal components. (b) Vertical component.

Figure 30: NEA landing MC simulation, waypoint improved maneuver case: final velocity distribution.

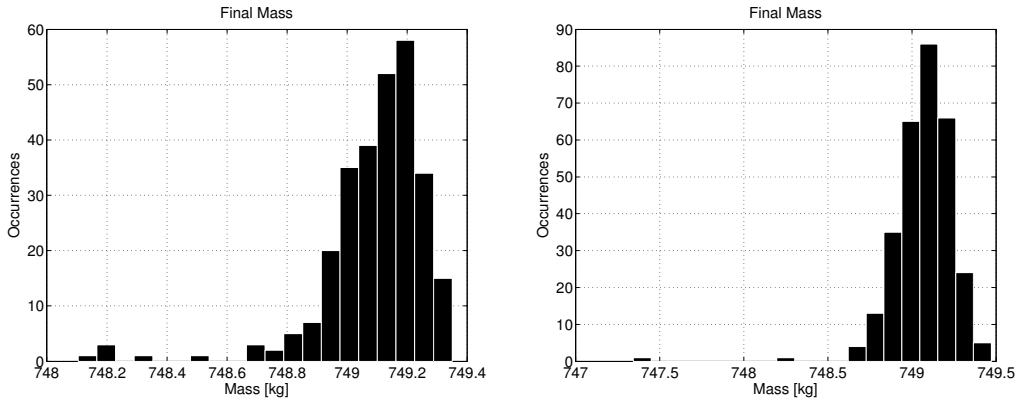

(a) Single maneuver case.

(b) Waypoint case.

Figure 31: NEA landing MC simulation: comparison between single maneuver and waypoint improved trajectory.